PROCEEDINGS A

royalsocietypublishing.org/journal/rspa

Research

Check for updates

Article submitted to journal

Subject Areas:
Condensed matter physics, Materials science, Computational physics, Nanotechnology

Keywords:
Graphene, Thermal conductivity, Twisted graphene, Strained graphene

Author for correspondence:
Qingxiang Ji, Changguo Wang
e-mail: qingxiang.ji@femto-st.fr, wangcg@hit.edu.cn

Emergence of Thermal Magic Strain and Magic Angle in Moiré Bilayer Graphene

Bohan Li[1,2], Qingxiang Ji[1,3], Jinliang Wang[1,3], Changguo Wang[1], Muamer Kadic[3], Krzysztof K. Dudek[2]

[1]National Key Laboratory of Science and Technology on Advanced Composites in Special Environments, Harbin Institute of Technology, Harbin, 150001, PR China
[2]Institute of Physics, University of Zielona Gora, ul. Szafrana 4a, 65-516 Zielona Gora, Poland
[3]Université Marie et Louis Pasteur, SUPMICROTECH, CNRS, Institut FEMTO-ST, Besançon, France

Despite intense studies focused on graphene-based systems, several facets of their behavior remain unexplored. One such aspect is the effect that some forms of mechanical deformation have on the thermal conductivity of a multilayer graphene. To address this aspect, we investigate the thermal conductivity of bilayer graphene subjected to uniform biaxial strain and interlayer twist using non-equilibrium molecular dynamics methods. A pronounced local minimum in thermal conductivity is identified at a characteristic strain ($S \approx 0.019$) and twist angle ($\theta \approx 1.1°$), which we term the thermal magic strain and thermal magic angle, respectively. The persistence of these extrema under variations in temperature, interlayer distance, and size confirms their intrinsic structural origin. Meanwhile, these extrema arise from deformation-induced moiré superlattices, which generate spatially heterogeneous atomic stress and enhance phonon scattering. The competition between increasing scattering-site density and stress delocalisation leads to a non-monotonic thermal response. Phonon density of states analysis further supports this mechanism and confirms the role of geometric mismatch in tuning heat transport. Our findings establish geometric modulation as an effective strategy for tuning lattice thermal transport and extend the concept of magic-strain physics to phonon-mediated heat conduction in two-dimensional materials.

© The Authors. Published by the Royal Society under the terms of the Creative Commons Attribution License http://creativecommons.org/licenses/by/4.0/, which permits unrestricted use, provided the original author and source are credited.

THE ROYAL SOCIETY PUBLISHING

1. Introduction

Bilayer graphene has emerged as a prototypical platform for exploring structure–property relationships in low-dimensional materials [1–5]. The weak van der Waals coupling between adjacent layers permits controlled modification of stacking configurations through external perturbations, including in-plane strain and rotational misalignment [6–10]. Such geometric modulation generates long-wavelength moiré superlattices, which introduce spatially varying interlayer registry and give rise to emergent electronic [11–13], mechanical [14–17], and vibrational phenomena [18–20] beyond those found in monolayer graphene.

In particular, twisted bilayer graphene has attracted significant attention following the observation of correlated electronic states near specific twist angles, commonly termed "magic angles" [21–23]. At these characteristic geometries, interlayer hybridisation and band reconstruction produce flat electronic bands and enhanced interaction effects [24–26]. Compared with rotational misalignment, uniform in-plane strain provides a mechanically accessible means of modulating lattice periodicity and similarly induces interlayer lattice mismatch [27–29]. In both cases, the resulting moiré pattern fundamentally alters the local stacking environment and modifies interatomic interactions over length scales much larger than the primitive lattice constant [30,31].

While the electronic consequences of moiré superlattices have been extensively investigated, their influence on lattice dynamics and thermal transport remains comparatively less understood. TC in graphene is governed predominantly by lattice vibrations [32–34], and is highly sensitive to phonon dispersion [35–37], anharmonicity [38,39], and scattering processes [40–42]. In bilayer systems, spatial modulation of stacking registry produces non-uniform interlayer coupling, leading to position-dependent force constants and heterogeneous stress distributions [43–45]. These structural inhomogeneities may induce phonon mode renormalisation [46], spectral redistribution [47], and enhanced scattering [48] at stacking boundaries or saddle-point regions. In addition, interlayer coupling has been recognized as a key structural parameter that can significantly influence the thermal properties of two-dimensional materials. It governs the strength of interlayer interactions and thus directly affects phonon dispersion, scattering processes, and cross-plane heat transport. The magnitude of interlayer coupling can be effectively tuned by applying external pressure [49,50] or by varying the interlayer distance. However, despite its importance, the role of interlayer spacing in modulating moiré superlattice structures and their associated thermal transport properties remains insufficiently explored.

To elucidate the relationship between moiré-induced structural modulation and thermal transport, a methodology capable of resolving both atomic-scale interactions and long-wavelength superlattice effects is required. Continuum models [51–53], while effective for describing macroscopic elasticity, do not fully capture the atomistic force redistribution and phonon scattering arising from local stacking variations. Conversely, first-principles [54–56] approaches are often limited by the large moiré unit cells associated with small scaling factors or twist angles. Non-equilibrium molecular dynamics [57–59] simulations provide a suitable framework in this context, enabling direct evaluation of heat flux, temperature gradients, and phonon-mediated energy transport while explicitly accounting for interatomic interactions and stress heterogeneity across extended supercells.

In this work, we investigate the TC of strained and twisted bilayer graphene using non-equilibrium molecular dynamics simulations. We primarily focus on bilayer graphene, where one layer is subjected to a uniform in-plane strain, and this deformation mode is fundamentally distinct from both interlayer twisting [60] and out-of-plane strain [49,50]. The selection of this specific type of mechanical deformation stems from the fact that it is potentially feasible from the perspective of future experiments and that its effect on the thermal conductivity remains mostly unexplored. In our study, we present our results in the context of more established bilayer graphene models such as twisted bilayer graphene. However, while we devote most of our attention to the concept of strained graphene and use other types of

deformed bilayer systems for comparative purposes, we also provide some novel aspects of the analysis focused on TBG. Even though in previous work [8], the author also reports a thermal magic angle in twisted bilayer graphene, in our work, we extend this concept to strain-induced moiré systems and modulate interlayer coupling strength through changing interlayer distance. Through our studies, a pronounced local minimum is identified at a characteristic scaling factor and twist angle, respectively. These extrema remain robust under variations in interlayer distance, system size, and temperature, indicating an intrinsic structural origin. Then, analysis of atomic stress distributions and phonon density of states reveals that this behaviour arises from the competition between the increasing density of moiré-induced scattering regions and the concurrent delocalisation of the stress field. The resulting non-monotonic evolution of phonon transport parameters gives rise to the observed TC minimum. Our results provide a unified physical picture linking moiré structural modulation, stress heterogeneity, phonon spectral redistribution, and thermal transport in bilayer graphene. These findings extend the concept of geometry-controlled emergent phenomena beyond electronic systems and highlight the fundamental role of structural modulation in governing lattice thermal transport in two-dimensional materials.

2. Models and Simulation methods

Models and simulation details. The pristine bilayer graphene structures are generated within the Large-scale Atomic/Molecular Massively Parallel Simulator (LAMMPS), and the length and width are taken as $L_x = L_y = 440$ Å, while the interlayer distance h is set as 7 Å. The interlayer distance is defined as the average out-of-plane separation between the two graphene layers, while all atoms are fully relaxed without any artificial constraints, thereby allowing natural out-of-plane corrugation to develop and be intrinsically accounted for. An aspect ratio of unity is retained throughout the study even when one of the layers is being deformed. The undeformed configuration corresponds to AB stacking [61], representing the stable equilibrium arrangement of bilayer graphene, as depicted in figure 1a. This pristine model is used as a reference to two types of deformed bilayer geometries that we analyze from the perspective of thermal conductivity (TC). The first one, i.e. the twisted bilayer graphene (TBG), is produced by prescribing a relative in-plane rotation of angle θ to the upper layer while constraining the lower layer (figure 1b). The second model corresponding to the strained bilayer graphene (SBG) is obtained by applying a uniform biaxial stretching to the upper layer, with the lower layer remaining fixed (figure 1c). In the case of such an idealized straining process, the aspect ratio of the deformed layer remains the same compared to that of the undeformed graphene sheet. Denoting the pristine and deformed C–C bond lengths by b_1 and b_2, respectively, the dimensionless scaling factor, which is later used in the quantitative analysis of the effect that strain has on TC, is defined as $S = (b_2 - b_1)/b_1$. In the case of TBG, the parameter quantifying the extent of mechanical deformation is the twist angle θ. For both types of mechanical deformation, the characteristic moiré length scales depend on the extent of the imposed deformation. For a rotational mismatch, it follows $a_{\mathrm{moire}} = a/2\sin(\theta/2)$ where $a = 2.45$ Å is the lattice constant of monolayer graphene. Under uniform biaxial strain, the effective superlattice periodicity can be written as $a_{\mathrm{moire}} = 100a(1+S)/\mathrm{gcd}(100(1+S), 100)$ where gcd(.,.) stands for the greatest common divisor. In all simulations, the lateral dimensions of the calculation domain are selected such that they considerably exceed the corresponding moiré wavelength. This choice prevents artificial commensurability effects associated with periodic boundary conditions and allows us to obtain TC in the latter part of our work. In figure 1(d, e), we show the top views of the SBG and TBG. The resulting patterns demonstrate that rotational and strain-induced mismatches give rise to qualitatively different moiré patterns.

In this paper, we use the non-equilibrium molecular dynamics (NEMD) method to calculate TC of all structures. Adaptive Intermolecular Reactive Empirical Bond Order (AIREBO) [62] is typically used for intralayer (covalent) bonds, while Lennard-Jones (LJ) [63] is used for interlayer (VdW) interactions. The cutoff of the LJ potential is chosen as 13Å, beyond which the weak interlayer Van der Waals interaction is negligible. During the simulation, the pristine

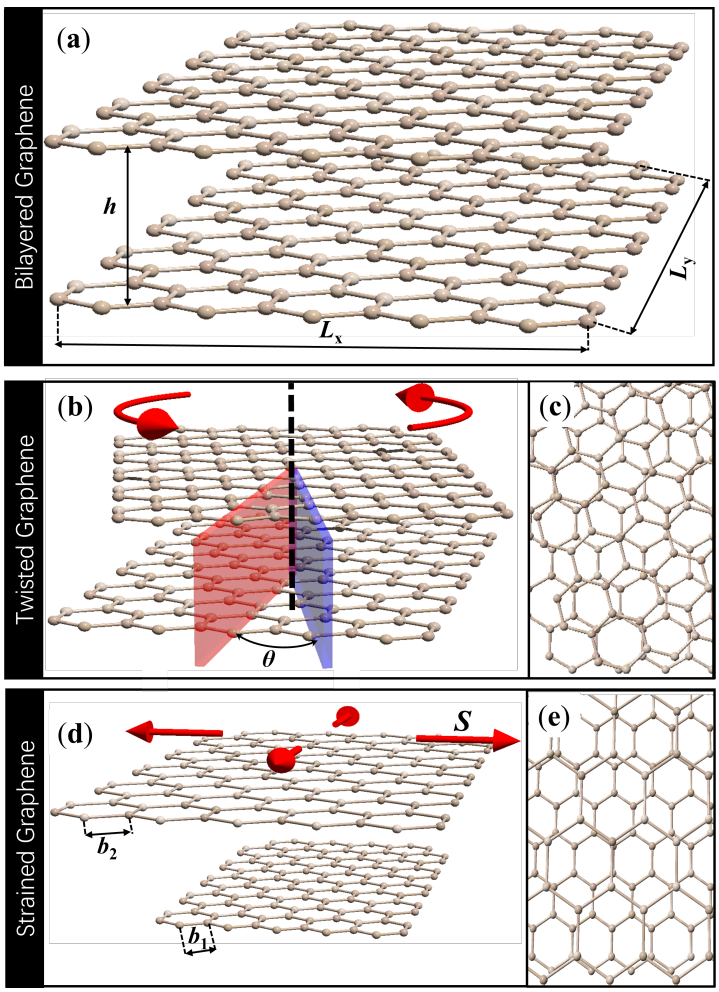


Figure 1. Schematic diagrams of bilayer graphene. (a) Pristine AB-stacked bilayer graphene. Here, h is the interlayer distance, L_x and L_y are the length and width, respectively. (b) Twisted bilayer graphene. Here, θ represents the twist angle. (c) Strained bilayer graphene under uniform biaxial stretch applied to the top layer. The pristine and deformed C–C bond lengths are denoted by b_1 and b_2, respectively, and the scaling factor is defined as $S = (b_2 - b_1)/b_1$. Top views of (d) strained and (e) twisted bilayer graphene are also depicted. Different moiré patterns give rise to distinct distributions of phonon scattering sites, thereby influencing the resulting thermal transport behaviour.

temperatures T of both SBG and TBG are kept at 300K and the timesteps are set as 1 fs. For SBG, due to the stiffness of graphene, the structure with a scaling factor S larger than 0.15 are not realistic since graphene sheets would get damaged [64]. In addition, the strain distribution in SBG is symmetric, which allows for retaining hexagonal symmetry. For TBG, due to the symmetry of graphene, the structure with a twist angle θ larger than 30° is identical to the structure with the angle $60°-\theta$. Given the above, for the two types of structures investigated in this study, we only consider the scaling factors from 0 to 0.15 for SBG and twist angles from 0° to 30° for TBG.

NEMD simulations. The TC is evaluated using the non-equilibrium molecular dynamics (NEMD) method. In this work, a stationary temperature gradient is imposed by introducing heat flux into the system, thereby driving it away from thermal equilibrium. The resulting non-equilibrium steady state enables the calculation of TC. The atomic heat flux between the heat

source and heat sink in the graphene sheets can be expressed as:

$$J = \frac{1}{V}\left[\sum_i e_i v_i - \sum_i s_i v_i\right]. \tag{2.1}$$

Here, J denotes the heat flux between the heat source and sink, V is the system volume, e represents total energy, v is the atomic velocity vector, and s denotes the atomic virial stress tensor. The cumulative energy exchanged between the heat source and heat sink is recorded to determine the steady-state heat flux and to construct the corresponding temperature gradient profile. The atomic temperature from the kinetic energy can be expressed as:

$$\sum_i \epsilon_i = \frac{n}{2} k_{\mathrm{B}} N T, \tag{2.2}$$

where i denotes atomic number, ϵ is the kinetic energy, n is the number of spatial degrees of freedom ($n = 3$ for a three dimensional system), N is the total atomic number within the calculation region and k_{B} is Boltzmann's constant.

The computational domain is partitioned into 100 slabs along the x-direction to resolve the spatial temperature profile. The local temperature in each slab is obtained from the atomic kinetic energy, allowing the temperature gradient $\partial T/\partial x$ to be determined from the steady-state profile. To eliminate the translation of the entire system, atoms within 10 Å from both ends of the graphene sheet along the x-direction are constrained. Thermal equilibration is first performed using a Nosé–Hoover thermostat at $T = 300$ K for 1 ns to establish a stable initial configuration. Subsequently, the heat source and heat sink are introduced by maintaining two regions at temperatures $T + 50$ K and $T - 50$ K, respectively. The imposed temperature difference drives a constant heat flux through the system. After reaching a non-equilibrium steady state, the dynamics are propagated within the microcanonical (NVE) ensemble, where total energy is conserved. The cumulative energy exchange between the heat source and heat sink is monitored over a total simulation time of 10 ns to extract the stationary heat flux. Throughout the simulations, the velocity-Verlet algorithm [65], a standard integration scheme in classical molecular dynamics, is used. The TC of bilayer graphene is then evaluated from Fourier's law as:

$$k = \frac{J \partial x}{A_c t\, \partial T}. \tag{2.3}$$

Here, k denotes the TC, $\partial T/\partial x$ is the temperature gradient along the x-direction, A_c is the effective cross-sectional area, t is the total simulation time.

3. Results and discussions

The TC of undeformed bilayer graphene at $T = 300$ K, $L_{\mathrm{x}} = 440$ Å and $h = 7$Å is first evaluated as $k = 1638$ W/(mK) using equation 2.3. The relative reduction in TC is defined as $\kappa = (k_1 - k)/k$, where k_1 denotes the TC of the lattice mismatch structures. For SBG, the TC generally decreases with increasing scaling factor S. However, a non-monotonic behaviour is observed, characterised by a local minimum in the vicinity of $S = 0.019$. Beyond this value, the TC increases and reaches a local maximum near $S = 0.022$ at h=10 Å followed by a further decrement at larger scaling factor. At $S = 0.15$, the maximum relative reduction reaches approximately 45%, as shown in figure 2a. In our previous work [66], $S = 0.019$ is identified as a characteristic strain associated with anomalous electronic transport behaviour. By analogy, this strain is here referred to as thermal magic strain, corresponding to local minimum value in TC. We emphasize that the present use of the term 'magic' refers to extremal behaviour in phonon transport and does not imply the presence of flat electronic bands or correlated electronic states. The existence of this exotic behaviour is further examined under varying interlayer distances, lengths, and temperatures (figure 2(a–c)). The local minimum TC shifts towards larger scaling factors with increasing interlayer distance h, indicating that a series of characteristic magic-strain values emerges for different interlayer spacings, while remaining essentially insensitive to variations in length and temperature. These

observations suggest that the local minimum TC is an intrinsic consequence of strain-induced structural modulation. For TBG at $T = 300$ K and $L_x = 440$ Å, a similar local minimum TC is identified at $\theta = 1.1°$ while $h = 7$ Å, consistent with previous reports [8]. The corresponding angle increases with increasing interlayer distance. Moreover, in-plane rotation produces a more pronounced reduction in TC compared with uniform biaxial strain. At $\theta = 25°$ and $h = 10$ Å, the maximum relative decrement reaches approximately 55%.

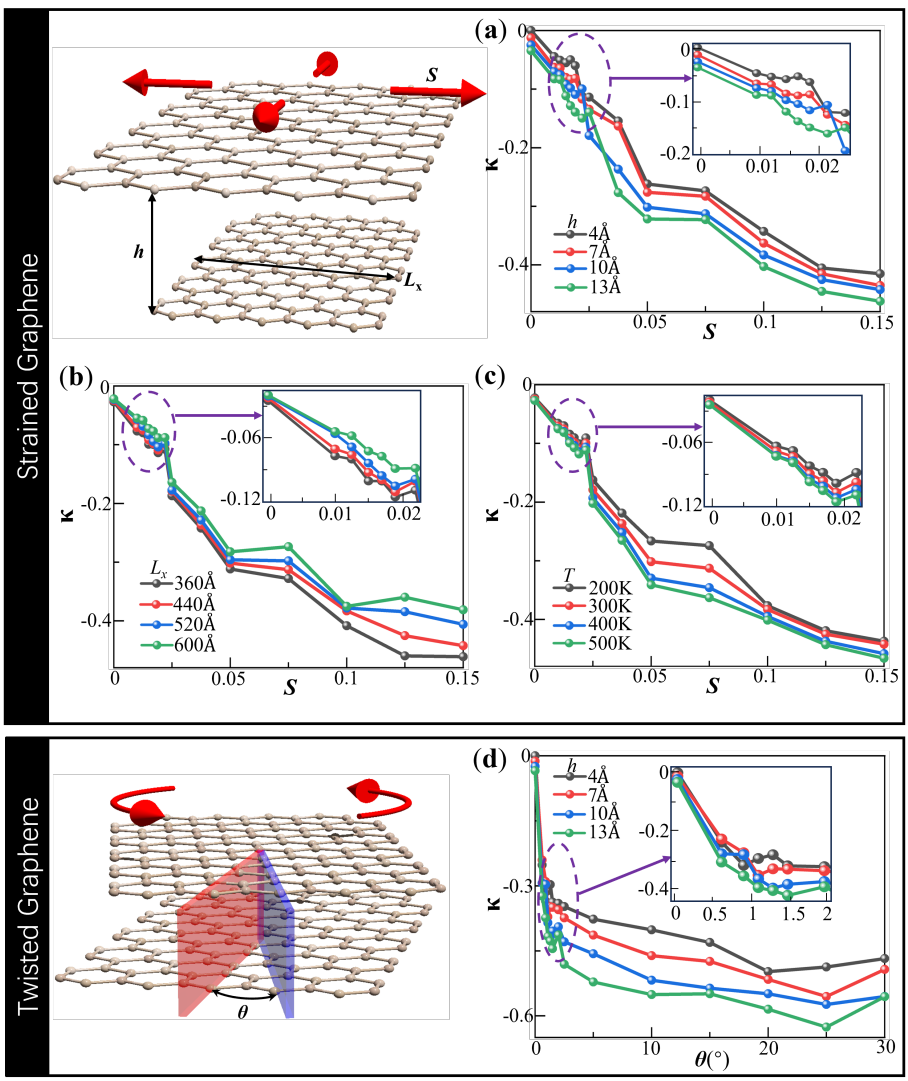


Figure 2. Variation of the relative reduction rate κ of TC. **Strained bilayer graphene**. Dependence of the decay rate of κ on the scaling factor S for different (a) interlayer distances h; (b) lengths L_x; (c) temperatures T. **Twisted bilayer graphene**. Dependence of the decay rate of κ on the twist angle θ for (d) different interlayer distances h. In both cases, a local minimum in TC is observed near $S = 0.019$ and $\theta = 1.1°$ under the indicated interlayer distances. This exotic behaviour is consistent with the magic-strain and magic-angle associated with analogous transitions in other reported properties.

In both SBG and TBG, the moiré superlattice is characterised by a large unit cell within which the local stacking configuration varies spatially. The stacking arrangements evolve continuously

from stable AB regions to less stable AA [67] and saddle-point (SP) [68] regions. This spatially modulated stacking arrangement alters the phonon scattering sites and leads to a reduction in TC. In addition, the non-uniform arrangement generates heterogeneous mechanical responses, manifested as a non-uniform atomic stress distribution. The emergence of the thermal magic strain and angle can be interpreted as a consequence of two competing effects. Increasing deformation enlarges the number of effective phonon scattering sites associated with the moiré modulation. At the same time, the atomic stress distribution becomes progressively delocalised, reducing the scattering strength associated with individual regions. The balance between these two mechanisms gives rise to the observed local minimum in TC.

The in-plane atomic stress exhibits a pronounced spatial dependence under uniform biaxial strain. The imposed deformation modifies the lattice periodic length of the stretched layer, generating a mismatch in in-plane periodic lengths between the fixed and deformed layers, as illustrated in figure 3(a-c). This lattice mismatch induces position-dependent interlayer interactions, resulting in alternating attractive and repulsive forces along the in-plane direction. Owing to the interlayer origin of these forces, the stress components in the stretched and fixed layers are oppositely directed with comparable magnitudes at corresponding spatial locations. Figure 3(d-f) illustrate the time-averaged normal stress along the x direction σ_{xx} of the SBG at $T = 300$ K, $h = 10$ Å and $L_{\mathrm{x}} = 440$ Å, corresponding to scaling factor $S = 0.019$, 0.022 and 0.05. The atomic-level stress tensor is defined as:

$$\sigma_{ab} = -m v_a v_b - W_{ab} \tag{3.1}$$

where a and b take on value x and y denote the in-plane Cartesian components. The first term represents the kinetic energy contribution to the atomic stress, where m denotes the mass of the reference atom. The second term corresponds to the virial contribution arising from interatomic interactions. The virial term accounts for both bonded and non-bonded interactions, including intra-layer and inter-layer forces within the bilayer system. It is expressed as [69]:

$$W_{ab} = \frac{1}{2}\sum_{n=1}^{N_p}(r_{3a}F_{3b} + r_{4a}F_{4b}) + \frac{1}{2}\sum_{n=1}^{N_b}(r_{3a}F_{3b} + r_{4a}F_{4b}) + K_{\mathrm{space}}(r_{ia}, F_{ib})\,,\ (i = 3, 4). \tag{3.2}$$

In equation 3.2, the first term is a pairwise energy contribution where n loops over the neighbors of a certain atom, r_3 and r_4 are the positions of the two atoms in the pairwise interaction, and F_1 and F_2 are the forces on the two atoms resulting from the pairwise interaction. The second term is a bond contribution of similar form for the N_b bonds which is part of certain atom. In addition, a reciprocal-space (KSpace) contribution is included to incorporate long-range Coulomb interactions. We observe that the center-to-center and edge-to-edge distances of the highlighted areas (r_1 and r_2) decrease as the scaling factor increases, implying an increased density of phonon scattering sites. In addition, the shear stress σ_{xy} at the same scaling factors can also be calculated using equation (3.1), as shown in figure 3(g–i). At small scaling factors, pronounced heterogeneity in the atomic stress distribution is observed for both σ_{xx} and σ_{xy}. These local stress variations decrease rapidly with increasing scaling factor and eventually become negligible. Notably, in contrast to σ_{xx}, the locations of the maximum and minimum values of σ_{xy} occur at different spatial positions.

In figure 3(j), at small scaling factors, the atomic stress distribution exhibits pronounced spatial heterogeneity. The in-plane atomic stress components are broadly distributed, spanning approximately -0.2 to 0.2 eV at $S = 0.019$. As the scaling factor increases, the distribution progressively narrows and approaches a Gaussian-like profile with reduced standard deviation. For $S > 0.01$, the distribution becomes comparable to that of the undeformed bilayer graphene. A similar trend is observed in TBG, as shown in figure 3(h). However, compared with SBG, the peak density of the stress distribution is significantly higher, indicating a more uniform stress distribution. Finally, we summarise the statistical distributions of the in-plane atomic stress in figure 3(j-k), and further demonstrate the gradual transition from heterogeneous to nearly homogeneous stress states with increasing deformation.

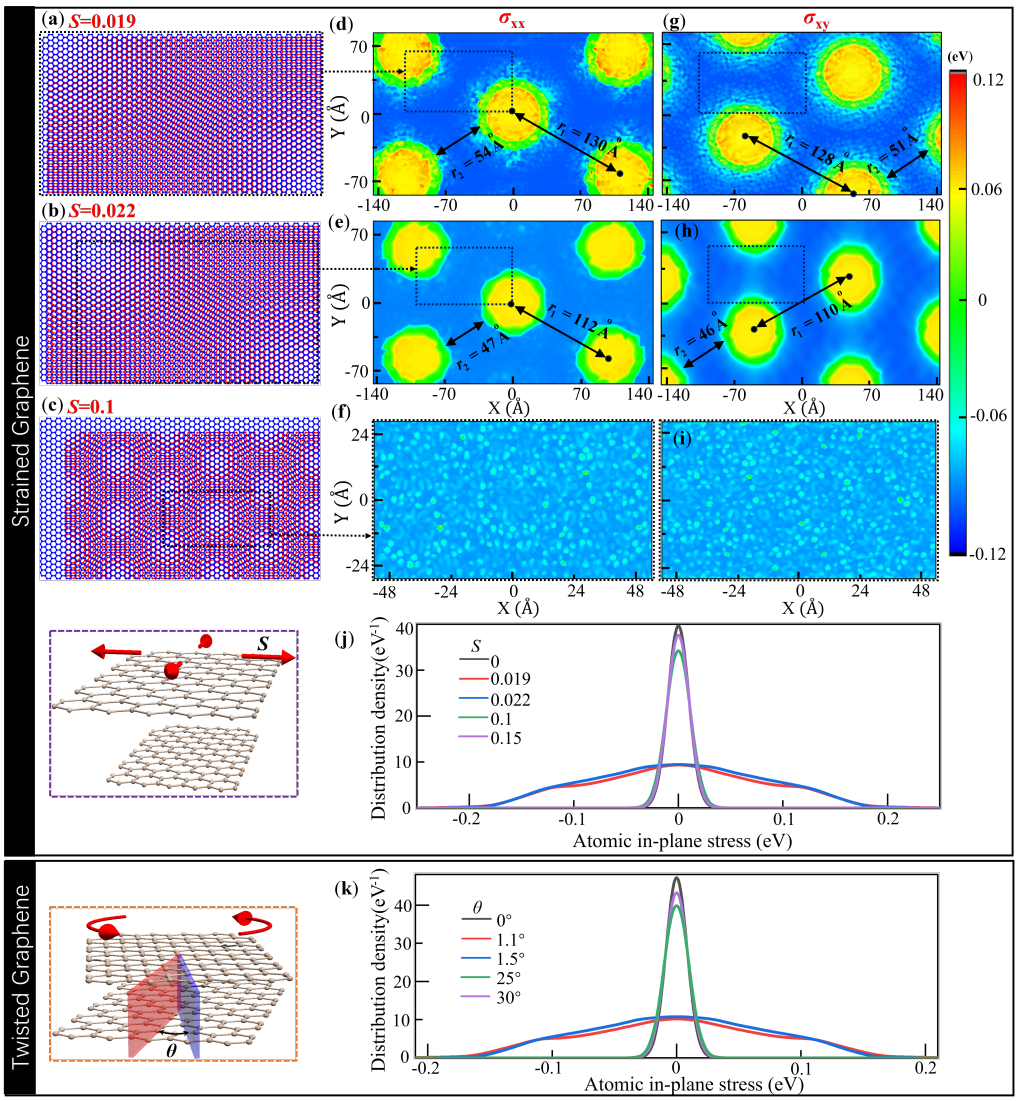


Figure 3. Atomic stress distributions in strained and twisted bilayer graphene. **Strained bilayer graphene** ($T = 300$ K, $h = 10$ Å, $L_x = 440$ Å). Moiré patterns corresponding to scaling factors (a) $S = 0.019$, (b) $S = 0.022$ and (c) $S = 0.1$. Spatial distributions of the normal stress along x direction σ_{xx} for different scaling factors (d) $S = 0.019$, (e) $S = 0.022$ and (f) $S = 0.1$. The corresponding spatial distributions of the shear stress σ_{xy} are presented for the same scaling factors in panels (g)–(i). For panels (d-f) and (e-g), the regions highlighted by black dashed boxes correlate with the moiré patterns shown in panels (a-c). (j) Distribution of atomic normal stress for all atoms under different scaling factors. **Twisted bilayer graphene** ($T = 300$ K, $h = 7$ Å, $L_x = 440$ Å). (k) Distribution of atomic normal stress for all atoms under different twist angles. In all cases, the averaged stress is shifted to zero for clarity. The stress distribution density is relatively small at low deformation (scaling factors and twist angles), and increases progressively with increasing deformation. At larger deformations, the normalised in-plane atomic stress distribution approaches a Gaussian profile with a reduced standard deviation, becoming comparable to the undeformed system.

The structure-induced spatial inhomogeneity in SBG and TBG introduces additional complexity into phonon transport compared with the undeformed system. In particular, the non-uniform stress distribution in SP regions modifies the local interatomic force constants, leading to shifts in phonon frequencies. Such stress-induced renormalisation of vibrational modes results

in spectral mismatches between SP regions and neighbouring stacking domains. Consequently, these regions act as effective phonon scattering centres [70], further reducing the overall TC. To quantify the influence of this scattering mechanism, the phonon density of states (PDOS) is calculated and analysed, as shown below:

$$\mathrm{PDOS}(\omega) = \frac{1}{N\sqrt{2\pi}} \int e^{-i\omega t} \left\langle \sum_{j=1}^{N} v_j(0) v_j(t) \right\rangle dt, \tag{3.3}$$

here, $\mathrm{NVACF} = \left\langle \sum_{j=1}^{N} v_j(0) v_j(t) \right\rangle$ denotes normalized velocity autocorrelation function (NVACF), ω is phonon frequency, v_j is the velocity vector of the j-th atom. As shown in figure 4, two prominent spectral features are observed: a low-frequency peak in the range 3–6 THz and a high-frequency peak between 50 and 55 THz. Unlike conventional three-dimensional materials, thermal transport in bilayer graphene is governed primarily by two mechanisms. The first is associated with the phonon frequency distribution, since TC can be approximately expressed as:

$$k \approx T^{-1} \left(\frac{\omega}{\omega_0} \right)^{\frac{\beta}{\alpha}}. \tag{3.4}$$

Here, T denotes the temperature, and ω represents the characteristic phonon frequency associated with the dominant spectral peak. The parameters α and β are functions determined by the interatomic potential and describe the anharmonicity of lattice vibrations. The second mechanism can be interpreted within the framework of lattice thermal transport theory, where the TC is expressed as

$$k = \sum_{m} C_v v_m l. \tag{3.5}$$

Here, m denotes the phonon modes at a given temperature, C_v denotes the specific heat capacity, v_m is the phonon group velocity, and l is the corresponding phonon mean free path. Both v_m and l are proportional to the spectral characteristics of the dominant PDOS peaks. In general, lattice thermal transport theory indicates that variations in group velocity and mean free path play a more significant role in determining TC than the phonon frequency shift [71]. As shown in figure 4a, the PDOS peak intensity at the thermal magic strain $S = 0.019$ is markedly lower than that of the undeformed case ($S = 0$) and the moderately strained case ($S = 0.022$). According to equation 3.5, this reduction in peak intensity corresponds to decreased phonon group velocity and mean free path, leading to a local minimum in TC near the thermal magic strain. For $S > 0.022$, the peak intensity exhibits an overall decreasing tendency with increasing scaling factor, consistent with the observed reduction in TC. Furthermore, increasing the interlayer distance and temperature, or decreasing the system length, leads to a decrement of peak intensity, indicating a corresponding decline in TC, as shown in figure 4(b-d). For twisted bilayer graphene, as shown in figure 4e, a similar local minimum in PDOS peak intensity is observed at $\theta = 1.1°$, corresponding to the thermal magic angle. However, in contrast to strained bilayer graphene, the evolution beyond the magic angle is non-monotonic. For example, the peak intensity at $\theta = 30°$ exceeds that at $\theta = 25°$, implying a higher TC at the larger twist angle. In addition, in-plane rotational deformation induces a leftward shift of the dominant PDOS peak, thereby further enhancing phonon scattering and contributing to the overall reduction in TC, as predicted by equation (3.5). Overall, the PDOS analysis is consistent with the TC trends presented in figure 2. While the present study focuses on phonon-mediated heat transport, the structural modulations identified here—such as moiré superlattices [72,73] and the associated spatial variation of atomic stress—may also have implications for electronic properties in bilayer graphene [74]. In particular, these structural features could influence interlayer coupling and lattice periodicity, which are known to play a role in the formation of flat electronic bands in moiré systems. Therefore, any possible interplay between phononic and electronic degrees of freedom remains speculative and will be further investigated in the future.

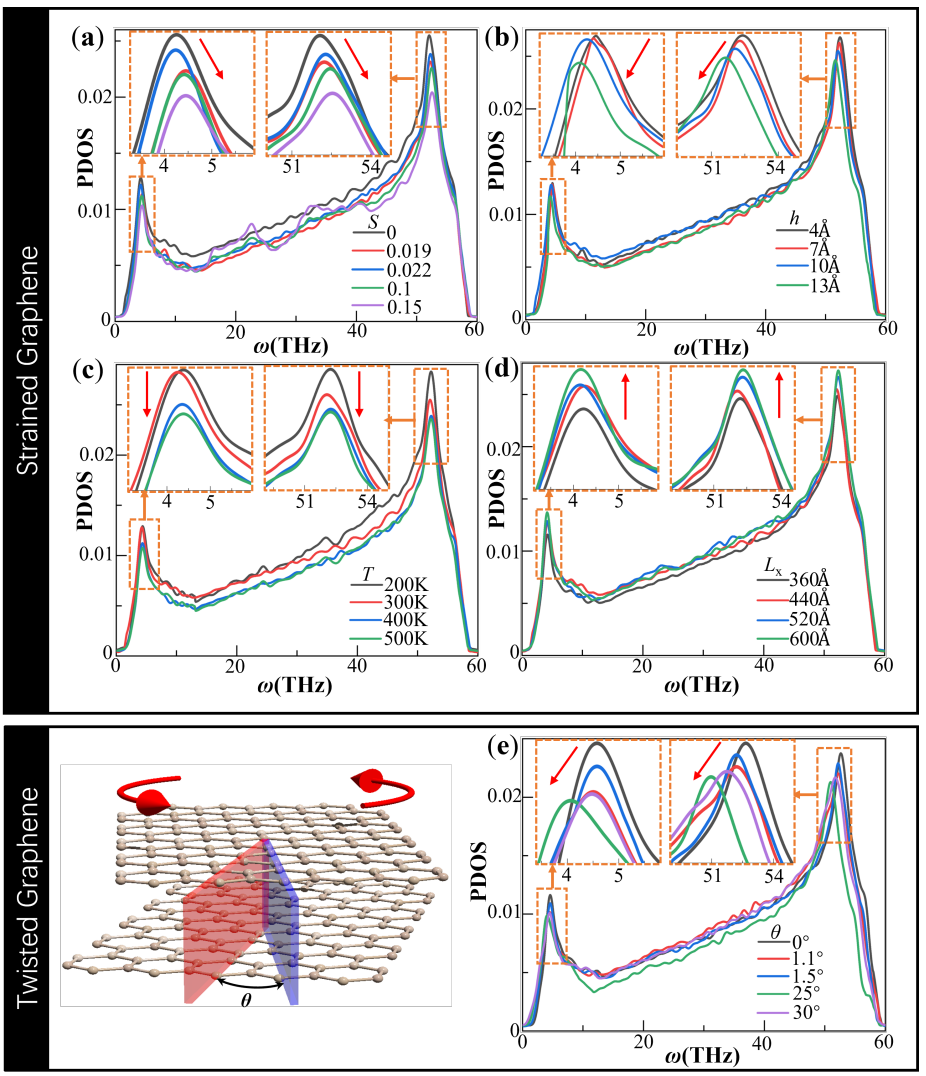


Figure 4. PDOS in strained and twisted bilayer graphene. **Strained bilayer graphene**. PDOS under variations of (a) scaling factors S ($T = 300$ K, $L_x = 440$ Å, $h = 10$ Å); (b) interlayer distances h ($T = 300$ K, $L_x = 440$ Å, $S = 0$); (c) temperatures T ($L_x = 440$ Å, $h = 10$ Å, $S = 0$) and (d) lengths L_x ($T = 300$ K, $h = 10$ Å, $S = 0$). **Twisted bilayer graphene**. PDOS for different (e) twist angles θ ($T = 300$ K, $L_x = 440$ Å, $h = 7$ Å). The left and right insets show magnified views of the phonon frequency ranges 3–6 THz and 50–55 THz, respectively. Variations in the peak values within these magnified views correlate with the deformation-dependent modification of phonon scattering sites, and are consistent with the corresponding changes in TC observed for both strained and twisted bilayer graphene.

4. Conclusion

In summary, a thermal magic strain $S = 0.019$ and thermal magic angle $\theta = 1.1°$ are identified as quantities that define the extent of the two considered types of deformation at which the TC for the bilayer graphene exhibits a local minimum. We further identify that these results are strongly dependent on the interlayer distance, which plays a crucial role in modulating interlayer interactions and, consequently, phonon transport behaviour. Variations in interlayer spacing alter the strength of van der Waals coupling, leading to significant changes in moiré pattern characteristics. As a result, the interlayer distance not only influences the magnitude of

thermal conductivity but also governs the emergence and position of the thermal magic strain and thermal magic angle. Then, we managed to show that the application of uniform biaxial strain or relative in-plane rotation modifies the stacking configuration of the bilayer graphene, giving rise to spatially heterogeneous atomic stress distributions. The resulting stress localization enhances phonon scattering and reduces TC. For small twist angles and scaling factors, the stress field becomes progressively more delocalized as the deformation increases, which weakens the scattering strength associated with an individual scattering region. Simultaneously, the number of such regions increases with increasing twist angle or scaling factors. The interplay between the decreasing scattering strength per site and the increasing density of scattering sites leads to the emergence of the observed exotic behaviour in TC. PDOS analysis further supports this interpretation by revealing deformation-induced modifications in peak value consistent with enhanced scattering. Though branch-specific contributions cannot be resolved within the present framework, we will consider to build a more comprehensive model to capture polarization-resolved or branch-resolved information, which would further clarify which modes are most strongly affected near the thermal magic strain and magic angle. These results indicate that controlled geometrical mismatch provides an additional parameter for tuning thermal transport in graphene-based systems and, more broadly, in two-dimensional crystalline materials.

Authors' contributions.

B.L.: Conceptualization, Formal analysis, Methodology, Writing - Original Draft,Validation. Q.J.: Writing - Editing, Validation, Supervision, Funding acquisition. J.W.: Software, Resources, Data curation, Investigation. C.W.: Supervision, Funding acquisition, Project administration. M.K.: Methodology, Formal analysis,Validation, Project administration. K.K.D: formal analysis, funding acquisition, project administration, supervision, validation, visualization, writing—review and editing.

All authors gave final approval for publication and agreed to be held accountable for the work performed therein.

Funding

B.L. gratefully acknowledges financial support from the China Scholarship Council (No.202506120076). K.K.D. acknowledges the support of the Polish National Science Centre (NCN) in the form of the grant awarded as a part of the SONATA 18 program, project No. 2022/47/D/ST5/00280 under the name "Active micro-scale mechanical metamaterials controlled by the external stimuli". This work was partially supported by a program of the Polish Ministry of Science under the title 'Regional Excellence Initiative', project no. RID/SP/0050/2024/1. M.K. acknowledges the support of the ANR OPTOBOTs project (ANR-21-CE33-0003), the ANR PNanoBot (ANR-21-CE33-0015), the French RENATECH network and its FEMTO-ST technological facility MIMENTO, and the French-Swiss SMYLE Network. Q.J. acknowledges the National Natural Science Foundation of China (12302169) and Marie Skłodowska-Curie Actions Postdoctoral Fellowships (101149710).

References

1. Tanaka M, Wang JÎj, Dinh TH, Rodan-Legrain D, Zaman S, Hays M, Almanakly A, Kannan B, Kim DK, Niedzielski BM et al.. 2025 Superfluid stiffness of magic-angle twisted bilayer graphene. *Nature* **638**, 99–105.
2. Hou Y, Zhou J, Xue M, Yu M, Han Y, Zhang Z, Lu Y. 2025 Strain Engineering of Twisted Bilayer Graphene: The Rise of Strain-Twistronics. *Small* **21**, 2311185.
3. Eder S, Hellner S, Forti S, Nordbotten J, Manson J, Coletti C, Holst B. 2021 Temperature-dependent bending rigidity of AB-stacked bilayer graphene. *Physical Review Letters* **127**, 266102.

4. Ji Q, Xue Z, Zhang Z, Cui Z, Kadic M, Wang C. 2023 Interlayer torsional sliding and strain localization in bilayer graphene. *Proceedings of the Royal Society A: Mathematical, Physical and Engineering Sciences* **479**.
5. Zheng X, Kamat AM, Krushynska AO, Cao M, Kottapalli AGP. 2022 3D printed graphene piezoresistive microelectromechanical system sensors to explain the ultrasensitive wake tracking of wavy seal whiskers. *Advanced Functional Materials* **32**, 2207274.
6. Dudek KK, Kadic M, Coulais C, Bertoldi K. 2025 Shape-morphing metamaterials. *Nature Reviews Materials* **10**, 783–798.
7. Gurtas Dogan S, Hasanirokh K, Mustafa O, Guvendi A. 2025 Twist-induced effects on Weyl pairs in magnetized graphene nanoribbons. *Proceedings of the Royal Society A: Mathematical, Physical and Engineering Sciences* **481**.
8. Cheng Y, Fan Z, Zhang T, Nomura M, Volz S, Zhu G, Li B, Xiong S. 2023 Magic angle in thermal conductivity of twisted bilayer graphene. *Materials Today Physics* **35**, 101093.
9. Jiang Z, Borodich FM, Kispayeva D, Osorio Mancilla JM, Jin X. 2025 Nonlinear compression of graphite: few-layer and bilayer graphene. *Proceedings of the Royal Society A: Mathematical, Physical and Engineering Sciences* **481**.
10. Alaee R, Farhat M, Rockstuhl C, Lederer F. 2012 A perfect absorber made of a graphene micro-ribbon metamaterial. *Optics express* **20**, 28017–28024.
11. Rai G, Crippa L, Călugăru D, Hu H, Paoletti F, De'Medici L, Georges A, Bernevig BA, Valentí R, Sangiovanni G et al.. 2024 Dynamical correlations and order in magic-angle twisted bilayer graphene. *Physical Review X* **14**, 031045.
12. Birkbeck J, Xiao J, Inbar A, Taniguchi T, Watanabe K, Berg E, Glazman L, Guinea F, von Oppen F, Ilani S. 2025 Quantum twisting microscopy of phonons in twisted bilayer graphene. *Nature* **641**, 345–351.
13. Lai X, Li G, Coe AM, Pixley JH, Watanabe K, Taniguchi T, Andrei EY. 2025 Moiré periodic and quasiperiodic crystals in heterostructures of twisted bilayer graphene on hexagonal boron nitride. *Nature materials* **24**, 1019–1026.
14. Xing H, Wang X, Xu C, Du H, Li R, Zhao Z, Qiu W. 2023 Spectral mechanical investigation of the elastic interface between a MoS2/graphene heterostructure and a soft substrate. *Carbon* **204**, 566–574.
15. Fu Z, Zhang W, Zhang Y, Chen H, Amer A. 2025 Mechanical behavior of twisted bilayer graphene and titanium nanocomposites. *International Journal of Mechanical Sciences* p. 110616.
16. Zhang Z, Krushynska AO. 2024 Shape morphing of tubular structures with tailorable mechanical properties. *Advanced Engineering Materials* **26**, 2300383.
17. Moghimimonfared R, Spaggiari A, Grasselli L, Mizzi L. 2025 Hexagonal tessellation-based mechanical metamaterials. *Extreme Mechanics Letters* **77**, 102356.
18. Liu X, Peng R, Sun Z, Liu J. 2022 Moiré phonons in magic-angle twisted bilayer graphene. *Nano letters* **22**, 7791–7797.
19. Amin M, Siddiqui O, Abutarboush H, Farhat M, Ramzan R. 2021 A THz graphene metasurface for polarization selective virus sensing. *Carbon* **176**, 580–591. (https://doi.org/10.1016/j.carbon.2021.02.051)
20. Han T, Bai X, Gao D, Thong JT, Li B, Qiu CW et al.. 2014 Experimental demonstration of a bilayer thermal cloak. *Phys. Rev. Lett* **112**, 054302.
21. Cao Y, Fatemi V, Fang S, Watanabe K, Taniguchi T, Kaxiras E, Jarillo-Herrero P. 2018a Unconventional superconductivity in magic-angle graphene superlattices. *Nature* **556**, 43–50.
22. Cao Y, Fatemi V, Demir A, Fang S, Tomarken SL, Luo JY, Sanchez-Yamagishi JD, Watanabe K, Taniguchi T, Kaxiras E et al.. 2018b Correlated insulator behaviour at half-filling in magic-angle graphene superlattices. *Nature* **556**, 80–84.
23. Park JM, Cao Y, Xia LQ, Sun S, Watanabe K, Taniguchi T, Jarillo-Herrero P. 2022 Robust superconductivity in magic-angle multilayer graphene family. *Nature Materials* **21**, 877–883.
24. Li Q, Zhang H, Wang Y, Chen W, Bao C, Liu Q, Lin T, Zhang S, Zhang H, Watanabe K et al.. 2024 Evolution of the flat band and the role of lattice relaxations in twisted bilayer graphene. *Nature Materials* **23**, 1070–1076.
25. Yu Y, Zhang K, Parks H, Babar M, Carr S, Craig IM, Van Winkle M, Lyssenko A, Taniguchi T, Watanabe K et al.. 2022 Tunable angle-dependent electrochemistry at twisted bilayer graphene with moiré flat bands. *Nature chemistry* **14**, 267–273.
26. Jiang C, Baggioli M, Jiang QD. 2024 Engineering flat bands in twisted-bilayer graphene away from the magic angle with chiral optical cavities. *Physical Review Letters* **132**, 166901.

27. Hu H, Rai G, Crippa L, Herzog-Arbeitman J, Călugăru D, Wehling T, Sangiovanni G, Valentí R, Tsvelik AM, Bernevig BA. 2023 Symmetric Kondo lattice states in doped strained twisted bilayer graphene. *Physical review letters* **131**, 166501.
28. Wan X, Sarkar S, Sun K, Lin SZ. 2023 Nearly flat Chern band in periodically strained monolayer and bilayer graphene. *Physical Review B* **108**, 125129.
29. Grima JN, Winczewski S, Mizzi L, Grech MC, Cauchi R, Gatt R, Attard D, Wojciechowski KW, Rybicki J. 2015 Tailoring Graphene to Achieve Negative Poisson's Ratio Properties. *Advanced Materials* **27**, 1455–1459. (https://doi.org/10.1002/adma.201404106)
30. de Jong TA, Benschop T, Chen X, Krasovskii EE, de Dood MJ, Tromp RM, Allan MP, Van der Molen SJ. 2022 Imaging moiré deformation and dynamics in twisted bilayer graphene. *Nature Communications* **13**, 70.
31. Ren YN, Zhan Z, Liu YW, Yan C, Yuan S, He L. 2023 Real-space mapping of local subdegree lattice rotations in low-angle twisted bilayer graphene. *Nano Letters* **23**, 1836–1842.
32. Li Q, Zheng Y, Wang H, Liu X, Lin M, Sui X, Leng X, Liu D, Wei Z, Song M et al.. 2025 Graphene-polymer reinforcement of perovskite lattices for durable solar cells. *Science* **387**, 1069–1077.
33. Xu M, Bao DL, Li A, Gao M, Meng D, Li A, Du S, Su G, Pennycook SJ, Pantelides ST et al.. 2023 Single-atom vibrational spectroscopy with chemical-bonding sensitivity. *Nature Materials* **22**, 612–618.
34. Zhu R, Liu X, Hu G, Sun C, Huang G. 2014 A chiral elastic metamaterial beam for broadband vibration suppression. *Journal of Sound and Vibration* **333**, 2759–2773.
35. Li A, Zeiger PM, He Z, Xu M, Pennycook SJ, Rusz J, Zhou W. 2024 Systematic absences of optical phonon modes in phonon dispersion measured by electron microscopy. *Physical Review Letters* **133**, 046101.
36. Ahmed S, Alam S, Jain A. 2023 Understanding phonon thermal transport in twisted bilayer graphene. *Physical Review B* **108**, 235202.
37. Yang L, Zhang Q, Hu G, Yang N. 2023 Deformation insensitive thermal conductance of the designed Si metamaterial. *Applied Physics Letters* **123**.
38. Guo X, Tian Q, Wang Y, Liu J, Jia G, Dou W, Song F, Zhang L, Qin Z, Huang H. 2022 Phonon anharmonicities in 7-armchair graphene nanoribbons. *Carbon* **190**, 312–318.
39. Han Z, Yang X, Sullivan SE, Feng T, Shi L, Li W, Ruan X. 2022 Raman linewidth contributions from four-phonon and electron-phonon interactions in graphene. *Physical Review Letters* **128**, 045901.
40. Gebert M, Bhattacharyya S, Bounds CC, Syed N, Daeneke T, Fuhrer MS. 2022 Passivating graphene and suppressing interfacial phonon scattering with mechanically transferred large-area Ga2O3. *Nano Letters* **23**, 363–370.
41. He J, Yu C, Lu S, Shan S, Zhang Z, Chen J. 2024 Complex role of strain engineering of lattice thermal conductivity in hydrogenated graphene-like borophene induced by high-order phonon anharmonicity. *Nanotechnology* **35**, 025703.
42. Hu G, Ou Q, Si G, Wu Y, Wu J, Dai Z, Krasnok A, Mazor Y, Zhang Q, Bao Q et al.. 2020 Topological polaritons and photonic magic angles in twisted α-MoO3 bilayers. *Nature* **582**, 209–213.
43. Dyck O, Yeom S, Lupini AR, Swett JL, Hensley D, Yoon M, Jesse S. 2023 Top-Down Fabrication of Atomic Patterns in Twisted Bilayer Graphene. *Advanced Materials* **35**, 2302906.
44. Li P, Wang Z, Cai G, Zhao Y, Deng Z, Wang B, Li Z, Ming X, Gao W, Xu Z et al.. 2026 High-performance graphene-based carbon fibres prepared at room temperature via domain folding. *Nature Materials* **25**, 191–198.
45. Chen K, Tang X, Jia B, Chao C, Wei Y, Hou J, Dong L, Deng X, Xiao TH, Goda K et al.. 2022 Graphene oxide bulk material reinforced by heterophase platelets with multiscale interface crosslinking. *Nature Materials* **21**, 1121–1129.
46. Emeis C, Jauernik S, Dahiya S, Pan Y, Jensen CE, Hein P, Bauer M, Caruso F. 2025 Coherent phonons and quasiparticle renormalization in semimetals from first principles. *Physical Review X* **15**, 021039.
47. Guandalini A, Senga R, Lin YC, Suenaga K, Ferretti A, Varsano D, Recchia A, Barone P, Mauri F, Pichler T et al.. 2023 Excitonic effects in energy-loss spectra of freestanding graphene. *Nano Letters* **23**, 11835–11841.
48. Sadeghi MM, Huang Y, Lian C, Giustino F, Tutuc E, MacDonald AH, Taniguchi T, Watanabe K, Shi L. 2023 Tunable electron–flexural phonon interaction in graphene heterostructures. *Nature* **617**, 282–286.

49. Duan F, Shen C, Zhang H, Qin G. 2022 Hydrodynamically enhanced thermal transport due to strong interlayer interactions: A case study of strained bilayer graphene. *Physical Review B* **105**, 125406.
50. Sun Z, Yuan K, Chang Z, Zhang X, Qin G, Tang D. 2019 Efficient thermal conductivity modulation by manipulating interlayer interactions: A comparative study of bilayer graphene and graphite. *Journal of Applied Physics* **126**.
51. Herzog-Arbeitman J, Wang Y, Liu J, Tam PM, Qi Z, Jia Y, Efetov DK, Vafek O, Regnault N, Weng H et al.. 2024 Moiré fractional Chern insulators. II. First-principles calculations and continuum models of rhombohedral graphene superlattices. *Physical Review B* **109**, 205122.
52. Liu H, Lee M, Šiškins M, Van Der Zant H, Steeneken P, Verbiest G. 2023 Tuning heat transport in graphene by tension. *Physical Review B* **108**, L081401.
53. Kern C, Miller OD, Milton GW. 2020 Tight bounds on the effective complex permittivity of isotropic composites and related problems. *Physical Review Applied* **14**, 054068.
54. Han Z, Ruan X. 2023 Thermal conductivity of monolayer graphene: Convergent and lower than diamond. *Physical Review B* **108**, L121412.
55. Tan ZW, Wang JS, Gan CK. 2011 First-principles study of heat transport properties of graphene nanoribbons. *Nano letters* **11**, 214–219.
56. Iwanowski K, Csányi G, Simoncelli M. 2025 Bond-network entropy governs heat transport in coordination-disordered solids. *Physical Review X* **15**, 041041.
57. Felix IM, Tromer RM, Machado LD, Galvão DS, Ribeiro LA, Pereira ML. 2024 Irida-graphene phonon thermal transport via non-equilibrium molecular dynamics simulations. *Nanoscale* **16**, 16430–16438.
58. Li B, Ji Q, Zhang Q, Wang C, Kadic M. 2024 Thermal nonreciprocity tuned by wrinkle patterns in graphene. *New Journal of Physics* **26**, 113020. (10.1088/1367-2630/ad91da)
59. Savin AV, Klinov AP. 2025 Wrinkles in graphene suspended on flat substrates: Structure and collapse under hydrostatic pressure. *Phys. Rev. B* **111**, 245403. (10.1103/PhysRevB.111.245403)
60. Kumar N, Chaudhuri A, Arya V, Bakli C, Bera C. 2023 Significantly reduced thermal conductivity and enhanced thermoelectric performance of twisted bilayer graphene. *Journal of Applied Physics* **134**.
61. Perello DJ, Lee S, Nai CT, Shin BG, Kim J, Park HY, Jeong HY, Zhao J, Vu QA, Lee SH et al.. 2016 Wafer-scale single-crystalline AB-stacked bilayer graphene. *Advanced Materials* **28**, 8177–8183.
62. Stuart SJ, Tutein AB, Harrison JA. 2000 A reactive potential for hydrocarbons with intermolecular interactions. *The Journal of chemical physics* **112**, 6472–6486.
63. Lebedeva IV, Knizhnik AA, Popov AM, Lozovik YE, Potapkin BV. 2011 Interlayer interaction and relative vibrations of bilayer graphene. *Physical Chemistry Chemical Physics* **13**, 5687–5695.
64. Wong JH, Wu BR, Lin MF. 2012 Strain effect on the electronic properties of single layer and bilayer graphene. *The Journal of Physical Chemistry C* **116**, 8271–8277.
65. Martys NS, Mountain RD. 1999 Velocity Verlet algorithm for dissipative-particle-dynamics-based models of suspensions. *Phys. Rev. E* **59**, 3733–3736. (10.1103/PhysRevE.59.3733)
66. Ji Q, Li B, Christensen J, Wang C, Kadic M. 2025 Phonon-mediated superconductivity in magic-strain bilayer graphene. *Physical Review B* **112**, 064507.
67. Rakhmanov A, Rozhkov A, Sboychakov A, Nori F. 2012 Instabilities of the AA-stacked graphene bilayer. *Physical review letters* **109**, 206801.
68. San-Jose P, Gorbachev R, Geim A, Novoselov KS, Guinea F. 2014 Stacking boundaries and transport in bilayer graphene. *Nano letters* **14**, 2052–2057.
69. Thompson AP, Plimpton SJ, Mattson W. 2009 General formulation of pressure and stress tensor for arbitrary many-body interaction potentials under periodic boundary conditions. *The Journal of chemical physics* **131**.
70. Wang H, Cheng Y, Nomura M, Volz S, Donadio D, Zhang X, Xiong S. 2021 Synergistic impeding of phonon transport through resonances and screw dislocations. *Physical Review B* **103**, 085414.
71. Wang C, Liu Y, Li L, Tan H. 2014 Anisotropic thermal conductivity of graphene wrinkles. *Nanoscale* **6**, 5703–5707.
72. Lu JZ, Zhu Z, Angeli M, Larson DT, Kaxiras E. 2022 Low-energy moiré phonons in twisted bilayer van der Waals heterostructures. *Physical Review B* **106**, 144305.
73. Miao W, Li C, Han X, Pan D, Dai X. 2023 Truncated atomic plane wave method for subband structure calculations of moiré systems. *Physical Review B* **107**, 125112.
74. Chen C, Nuckolls KP, Ding S, Miao W, Wong D, Oh M, Lee RL, He S, Peng C, Pei D et al.. 2024 Strong electron–phonon coupling in magic-angle twisted bilayer graphene. *Nature* **636**, 342–347.

75. Zhang X, Chen Z, Chen H, Xu L. 2021 Comparative studies of thermal conductivity for bilayer graphene with different potential functions in molecular dynamic simulations. *Results in Physics* **22**, 103894.
76. Kolmogorov AN, Crespi VH. 2005 Registry-dependent interlayer potential for graphitic systems. *Physical Review B—Condensed Matter and Materials Physics* **71**, 235415.
77. Leven I, Maaravi T, Azuri I, Kronik L, Hod O. 2016 Interlayer potential for graphene/h-BN heterostructures. *Journal of chemical theory and computation* **12**, 2896–2905.
78. Liu YY, Zhou WX, Tang LM, Chen KQ. 2014 An important mechanism for thermal rectification in graded nanowires. *Applied Physics Letters* **105**.
79. Martín MJ, Couso C, Rengel R. 2013 Velocity and momentum fluctuations in suspended monolayer graphene. In *2013 22nd International Conference on Noise and Fluctuations (ICNF)* pp. 1–4. IEEE.

Appendix

Atomic-stress distribution for TBG. To investigate the relationship between stress distributions and twist angles in TBG, we calculate the normal stress σ_{xx} and shear stress σ_{xy} at $T = 300$ K, $h = 7$ Å, and $L_x = 440$ Å. In the untwisted (AB-stacked) structure, the stress is negligibly small and uniformly distributed across the entire system. When a small twist angle is introduced, the normal stress σ_{xx} exhibits pronounced spatial variation. However, the magnitude and spatial heterogeneity of σ_{xx} gradually decrease as the twist angle increases. At sufficiently large twist angles, σ_{xx} becomes negligibly small again, as shown in figure A1(a–c). Similarly, the shear stress in the untwisted structure is very small and homogeneously distributed. The introduction of a small twist angle generates significant local shear stresses. As the twist angle increases, the spatial variation in shear stress weakens progressively. When the twist angle is large enough, the time-averaged shear stress becomes negligible, and the distribution returns to a nearly homogeneous state, as illustrated in figure A1(d–f).

Thermal conductivity of SBG with different interlayer potentials. Since the Kolmogorov–Crespi (KC) potential [75,76] and the interlayer potential (ILP) [77] are both widely used to describe weak interlayer interactions in two-dimensional materials, we further evaluate the TC of SBG using these potentials at $T = 300$ K, $h = 10$ Å, and $L_x = 440$ Å. The corresponding results are presented in figure A2. As shown in figure A2, although the absolute values of TC differ between the KC, ILP and LJ potentials, the overall trend remains consistent. Notably, the thermal magic strain appears at $S = 0.019$ for both potentials, in agreement with the results obtained using the LJ potential. Given the distinct formulations of these interlayer potentials, this consistency suggests that the thermal magic strain is an intrinsic property of SBG, rather than an artefact of a specific potential model.

Phonon lifetime of SBG and TBG. The normalized velocity autocorrelation function (NVACF), describes the temporal evolution of atomic velocity correlations and serves as a key quantity for analysing lattice dynamics. Its Fourier transform gives access to the PDOS. The rate at which the NVACF decays reflects the degree of anharmonic interactions and phonon scattering in the system. In this sense, a more rapid decay of the NVACF can be interpreted as an indication of reduced phonon lifetimes [78,79]. In figure A3(a,c), we calculate the NVACF for both SBG and TBG. The NVACF decays to nearly zero within approximately 1 ns, indicating that the system has reached a steady state. Based on this observation, we evaluate the average peak amplitude of the NVACF after 1 ns, which serves as a measure of the strength of the normalized velocity autocorrelation function (SNVACF), as shown in figure A3(b,d). The variations in SNVACF reflect deformation-dependent changes in phonon lifetimes and are consistent with the corresponding evolution of thermal conductivity observed in both SBG and TBG.

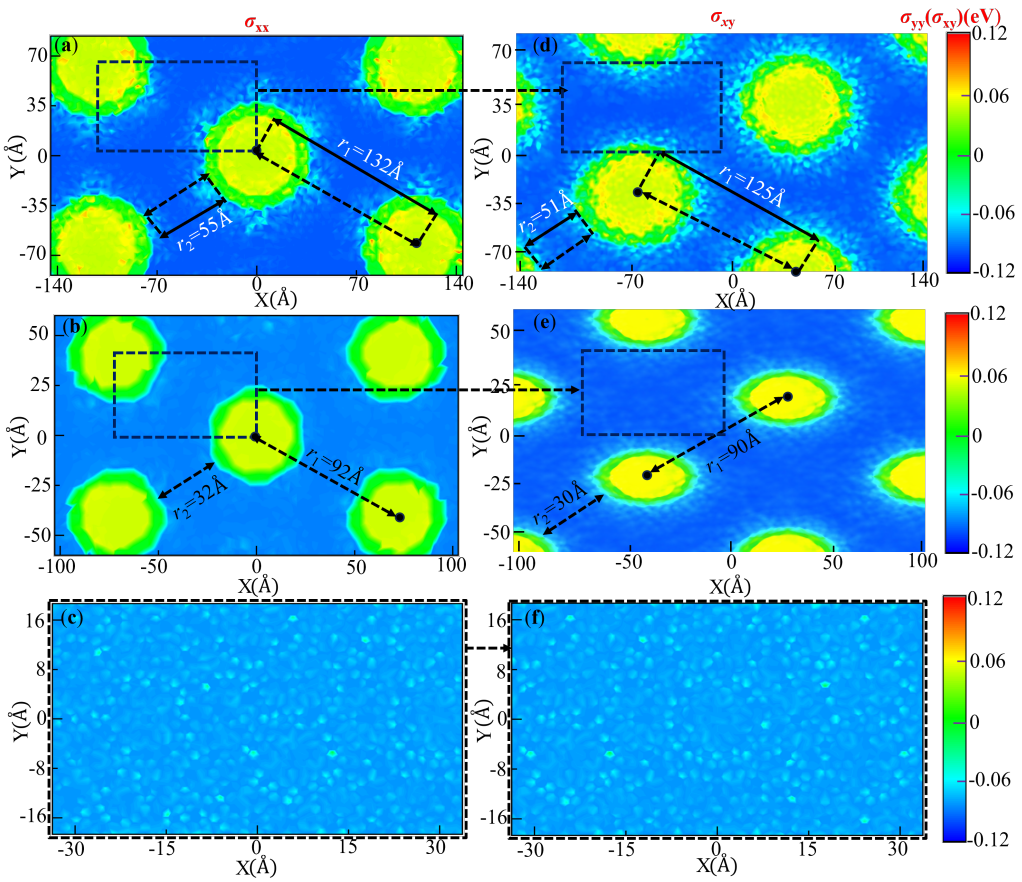


Figure A1. Atomic stress distributions in TBG ($T = 300$ K, $h = 7$ Å, $L_x = 440$ Å). Spatial distributions of the normal stress along x direction σ_{xx} for different twist angles (a) $\theta = 1.1°$, (b) $\theta = 1.5°$ and (c) $\theta = 25°$. The corresponding spatial distributions of the shear stress σ_{xy} are presented for the same twist angles in panels (d)–(f). In all cases, the averaged stress is shifted to zero for clarity.

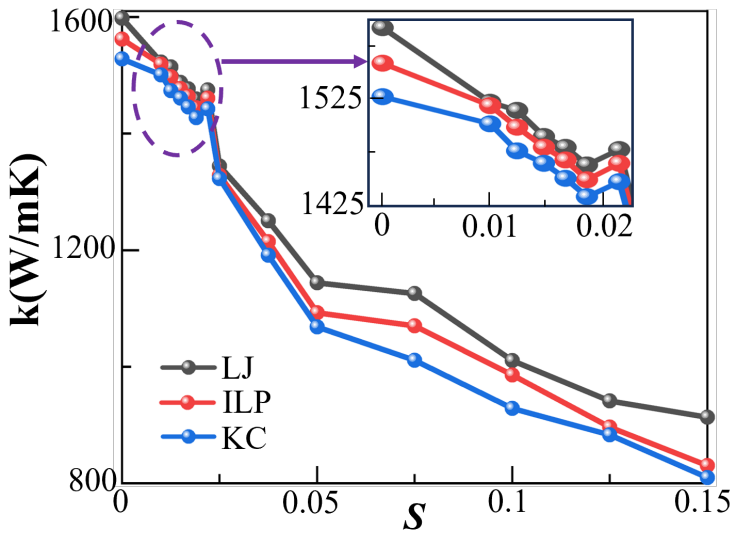


Figure A2. Thermal conductivity of strained bilayer graphene as a function of scaling factor with different interlayer potentials.

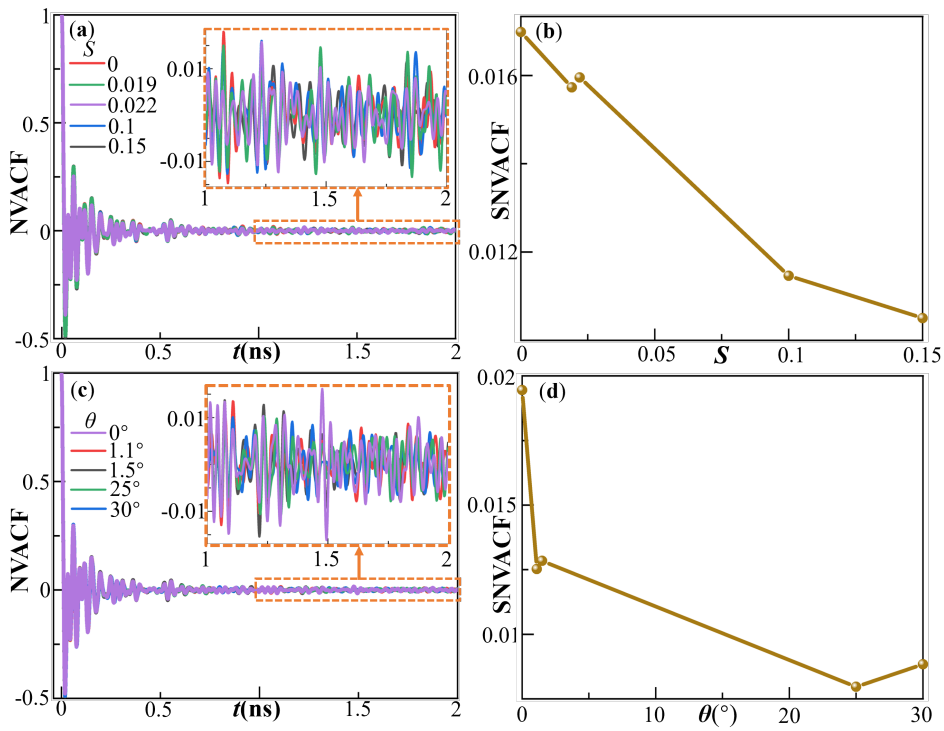


Figure A3. Normalized velocity autocorrelation function (NVACF) and its amplitude in strained and twisted bilayer graphene. **Strained bilayer graphene (SBG)** under variations of scaling factor S ($T = 300$ K, $L_x = 440$ Å, $h = 10$ Å): (a) NVACF and (b) the corresponding averaged peak amplitude (SNVACF). **Twisted bilayer graphene (TBG)** under variations of twist angle θ ($T = 300$ K, $L_x = 440$ Å, $h = 7$ Å): (c) NVACF and (d) SNVACF. Variations in SNVACF reflect deformation-dependent changes in phonon lifetimes and are consistent with the corresponding evolution of thermal conductivity in both SBG and TBG.